Confinement Reconstruction Unlocks Stable Ru Single Atoms-Doped IrO_x Anodes for Long-Term High-Rate CO_2 Electrolysis

Lei Wang[1Δ], Omar Lopez-Estrada[2Δ], Siyan Lu[1Δ], Cheng Du[1], Aman Soni[2], Xiyang Wang[1], Maoyu Wang[3], Hsiaotsu Wang[4, 5], Zuihar Singh[6], Ariel Tirado[4], Brant Billinghurst[4], Wei Wei[1], Baizhou Zhang[1], Zuolong Chen[1], Jian Wang[4], Jigang Zhou[4], Cheng-Jun Sun[3], Hua Zhou[3], Rodney D.L. Smith[6], Brian Kendall[7], David Sinton[8], Samira Siahrostami[9*], Yimin A. Wu[1,6*]

[1]Department of Mechanical and Mechatronics Engineering, Waterloo Institute for Nanotechnology, Materials Interfaces Foundry, University of Waterloo, Waterloo, Ontario N2L 3G1, Canada

[2]Department of Chemistry, University of Calgary, Calgary, Alberta, T2N 1N4 Canada

[3]X-Ray Science Division, Argonne National Laboratory, Lemont, IL 60439, USA

[4]Canadian Light Source, Saskatoon, SK S7N 2V3, Canada

[5]Bachelor's Program in Advanced Materials Science, Tamkang University, New Taipei City 25137, Taiwan

[6]Department of Chemistry, University of Waterloo, Ontario N2L 3G1, Canada

[7]Department of Earth and Environmental Sciences, University of Waterloo, Waterloo, Ontario N2L 3G1, Canada

[8]Department of Mechanical and Industrial Engineering, University of Toronto, Toronto, Ontario, M5T 0A3, Canada

[9]Department of Chemistry, Simon Fraser University, 8888 University Drive, Burnaby, British Columbia V5A 1S6, Canada

[Δ] Equal contributions

* Corresponding emails: samira_siahrostami@sfu.ca; yimin.wu@uwaterloo.ca

Abstract

IrO_2 is a commonly employed anode catalyst for CO_2 electrolysis in membrane electrode assembly (MEA) systems. However, under high current densities, its structural reconstruction leads to activity loss and stability

degradation, limiting industrial viability of CO_2 electrolysis. Herein, we demonstrated a confinement reconstruction strategy to precisely regulate the structural evolution during electrolysis. Ethylene glycol serves as a structural modulator, protecting the catalyst surface, suppressing soluble species formation, and promoting ordered structural evolution. Single-atom Ru acts as a stability enhancer, forming robust Ir–O–Ru bridging structures that facilitate an ordered transformation from a four-fold $[RuO_4]$/$[IrO_4]$ to a six-fold symmetry $[RuO_6]$/$[IrO_6]$ octahedral framework, thereby enhancing structural rigidity and long-term stability. As a result, in MEA-based CO_2 electrolysis, the catalyst achieves stable operation at 200 mA cm^{-2} for 480 h, maintaining a CO selectivity above 80%. Theoretical calculations further elucidate that the enhanced stability originates from the suppression of oxygen vacancy formation, making the lattice-oxygen-mediated mechanism (LOM) potentially less favorable. This work provides insights into the structural evolution of OER catalysts under high-current-density conditions, paving the way for large-scale CO_2 electrolysis commercialization.

Keywords: Electrocatalysis, CO_2 reduction, MEA, oxygen evolution reaction, structural reconstruction, stability, neutral electrolyte

Introduction

Electrocatalytic CO_2 reduction (eCO_2RR) to high-value chemicals and fuels using renewable energy presents a highly promising strategy to mitigate climate impact and achieve carbon neutrality[1-3]. Among various CO_2 electrolyzer, membrane electrode assembly (MEA) cell, as a dual-electrode zero-gap cell, offers significant advantages over flow cells. It effectively reduces cell resistance, enhances energy efficiency, and boosts cell stability, making MEA-based CO_2 electrolysis a more feasible and scalable approach for industrial-scale deployment[4, 5]. However, CO_2 electrolysis in MEA systems involves both the cathodic eCO_2RR and the anodic oxygen evolution reaction (OER)[6]. While eCO_2RR catalysts on the cathode side can efficiently and selectively convert CO_2 into specific products such as CO and ethylene[7-9], maintaining stable operation of the MEA system remains a key bottleneck for advancing the industrial implementation of eCO_2RR.

To address the stability challenges of MEA-based CO_2 electrolysis, while ensuring high product selectivity and activity of the eCO_2RR catalyst, the stability and activity of the OER catalyst are also of paramount importance. The conventional rutile-phase IrO_2 catalyst is widely recognized as a OER catalyst and has been extensively employed in eCO_2RR systems[7, 10-12]. However, under high current densities, it suffers from severe dissolution and structural degradation, significantly limiting the durability of the overall system[13-15]. Moreover, IrO_2 tends to transform into an amorphous yet highly active IrO_x phase under OER conditions, further compromising its structural stability[10, 16-18]. To overcome these problems, various structural engineering strategies have been developed, such as oxygen vacancy modulation. While these approaches can enhance OER activity, they may also lead to structural instability, shortening catalyst lifespan[19, 20]. Although previous studies have explored Ru-doped IrO_2, the mechanistic role of Ru, particularly in the structural reconstruction process under high current densities, remains unclear[21]. Considering the poor stability of IrO_x-based OER catalysts under acidic and alkaline

conditions[22-24], enhancing their stability in neutral electrolytes is a more promising approach for advancing practical CO_2 electrolysis. The key to overcoming this challenge lies in gaining a deep understanding of the reconstruction mechanisms of IrO_x-based catalysts and developing tailored material design strategies to achieve long-term stability under high current densities.

Herein, we introduced the concept of confinement reconstruction to regulate the structural evolution process of the IrO_x phase, thereby facilitating the formation of an ordered and ultrastable structure. Ethylene glycol (EG) serves as a structural modulator, effectively preventing excessive oxidation of Ir and the formation of disordered amorphous phases of Ir. Ru single atoms, acting as a dual-role dopant, not only serve as a stabilizing agent by forming robust Ir–O–Ru bridging structures, facilitating the structural reconstruction from 4-fold symmetry to 6-fold symmetry and enhancing structural rigidity, but also modulates the oxidation state of Ir, optimizing the electronic structure and improving the stability of catalytically active species. For CO_2-electrolysis in a MEA reactor, the Ru0.05mg/IrO_x catalyst demonstrated remarkable durability, sustaining continuous operation at a current density of 200 mA cm^{-2} for 480 h. Theoretical calculations further reveal that the selective incorporation of Ru single atoms within the IrO_2 lattice modulates oxygen adsorption behavior, tailors the electronic structure, and optimizes the scaling relations to minimize the energy gap between OER intermediates. This study provides an in-depth understanding of the catalyst evolution during the OER process and proposes novel strategies for optimizing OER catalysts under high current densities.

Materials and Methods

Chemicals

Titanium Fiber Felt (Ti mesh), approximately 53-56%, was purchased from Fuel cell store. Acetone, hydrochloric acid, oxalic acid dihydrate iridium (III) chloride hydrate, potassium carbonate, ruthenium (III) chloride hydrate, Iridium(IV) oxide, Ruthenium(IV) oxide, ethylene glycol, potassium bicarbonate, potassium hydroxide were purchased from Sigma with ACS grade. Gas Diffusion Layers Sigracet 39BB and Anion Exchange Membrane Sustainion® X37-50 Grade RT were purchased from Dioxide materials. Argon LaserStar 5.0 (99.9995%) and Carbon dioxide LaserStar 5.0 (99.999%) were from Praxair and Linde. Deionized water was used in the experiments. All reagents were used without further purification.

Fabrication of IrO_x/Ti electrodes by anodic electrodeposition

Before the electrodeposition process, Titanium Fiber Felt was firstly cut into 1 cm × 2 cm or 3 cm × 3 cm size and then fully washed with acetone, dilute HCl solution, and water, respectively. The IrO_x electrodeposition solution adopted the recipe reported by Zhang *et al.*[25]: Oxalic acid dihydrate (1 mmol) was combined with 30 ml of water containing 0.2 mmol of $IrCl_3$. The mixture was stirred for 10 minutes, and then K_2CO_3 (5 mmol) was added to raise the pH to 10-10.5. Next, the solution was diluted to a total volume of 50 ml, resulting in a final concentration of iridium ions of 4 mmol L^{-1}. This solution was maintained at a temperature of 40°C for approximately 5 days or

longer to achieve stabilization. Subsequently, it was stored as a stock solution at a temperature of 4°C. The electrodeposition was conducted using a three-electrode system, in which the Ti Fiber Felt served as the working electrode with a 1×1 cm^2 or 3×3 cm^2 working area. The reference electrode and counter electrodes were an Ag/AgCl electrode and a platinum wire, respectively. The electrochemical technique used for electrodeposition was the potentiometric method. The potentiometric electrodeposition was conducted in 25 mL electrodeposition solution with the Ti Fiber Felt as substrate under a potential of 0.0016A (versus Ag/AgCl) for 15, 30, 60, and 120 min. Finally, the samples were heat-treated in a tube furnace for 1 h at 500 °C under air.

Synthesis of Ru/IrO_x OER catalyst

Ru/IrO_x was synthesized by the galvanic replacement reaction. Typically, 2 or 40 mL x mg mL^{-1} (x=0, 0.005, 0.01, 0.05, 1) $RuCl_3$ solution was first prepared using ethylene glycol (EG) as solvent. EG acts as a reducing agent in the synthesis to reduce Ru^{3+} ions. Then Ti Fiber Felt with IrO_x nanoparticles was immersed into the solution under 80°C for 15min. After washing with isopropanol and water, the Ti Fiber Felt with IrO_x was dried by air flow. Ti mesh acts as a conductive electrode and does not participate in the OER reaction.

Preparation of gas diffusion electrode (GDE)

The silver was deposited on the 2.5×2.5 cm^2 GDL (Sigracet 39 BB) by AJA magnetic sputtering with a background pressure of 5×10^{-7} Torr. Ag metal was used as a bottom electrode which was deposited by direct current (DC) magnetic sputtering with the target Ag. The sputtering power was 100 W, the deposition pressure was 5 mTorr and the working gas was pure Ar of 12 sccm.

Electrochemical measurements

All electrochemical tests were measured on Metrohm Autolab PGSTAT 204 electrochemical workstations at room temperature with IR corrected. The OER stability and activity performance of the IrO_x and Ru/IrO_x catalyst with different Ru loading amounts in neutral conditions (0.5M $KHCO_3$ electrolytes) were systematically studied in a single compartment electrolytic cell. A three-electrode system was fabricated with the prepared IrO_x-based materials, platinum wire, and Ag/AgCl (in saturated KCl) electrode serving as the working electrode, the counter electrode, and the reference electrode, respectively. The synthesized Ti Fiber Felt with Ru/IrO_x catalyst directly served as the working electrode with an electrode holder. The surface area of the working electrode was controlled at 1 cm^2 in 25ml 0.5M $KHCO_3$ solution under an Ar gas environment. Linear sweep voltammetry (LSV) under a select potential range with 0.4V iR compensation was used for overpotential and activity measurement of the Ru/IrO_x catalytic OER reaction. After that, the chronoamperometry (I-T) test was used for stability measurements under the over potential at 10mA and 100mA for 30min or 60min. The Ru/IrO_x catalytic OER performance was evaluated using chronopotentiometry (P-T) tests under a selective potential for 12, 100, and 200 hours. Before the OER test, LSV curves were performed until the polarization curves achieved steady state. The electrochemically active surface area (ECSA) measurements were conducted using cyclic voltammetry (CV) scans at different rates from 10 to 50 mV s^{-1} with a 10 mV s^{-1} increment speed from 0.5 V_{RHE} to 0.7 V_{RHE}; within this potential range, the

Faradic process is excluded. All the potential values are presented in RHE unless otherwise stated using the following equation [26]:

$$E_{RHE} = E_{Ag/AgCl} + 0.197V + 0.059 \times pH \quad (1)$$

The ESCA is calculated by the following equation [26]:

$$A_{ECSA} = \frac{\text{Specific capacitance}}{40\ \mu F c m^{-2} c m^{-2}_{ECSA}} \quad (2)$$

The overpotential (η) is calculated from equation:

$$\eta(V) = E_{RHE} - 1.23V \quad (3)$$

The specific capacitance of the sample was obtained by CV. It was carried out at different scan rates in the range of 0.5 V_{RHE} to 0.7 V_{RHE}. 40 mF cm^{-2} is the specific capacitance of a flat surface for metallic and semiconducting materials with 1 cm^2 of the real surface area in the aqueous electrolyte[26].

OER performance measurement in MEA electrolyzers

The OER performance of Ru/IrO_x catalysts was evaluated in MEA electrolyzers coupling with the CO_2 reduction reaction. The electrolyzer setup is shown in **Figure 4A**. A potentiostat with a current booster (Metrohm Autolab, 10 A) was used to apply the current. To facilitate the electrochemical reactions, a commercially available CO_2 MEA electrolyzer from Dioxide Materials was utilized. The MEA electrolyzer consisted of flow field plates with a serpentine-shaped flow field of 5 cm^2, serving as the anode and cathode, enabling a continuous supply of 0.5 M $KHCO_3$ anolyte and humidified CO_2 to their respective electrodes. As for the specific components, the cathode utilized Ag gas diffusion electrode (GDE), the anode employed a Ti Fiber Felt with Ru/IrO_x catalyst, and a physically separated anion exchange membrane (Sustainion X37-50 membrane) separated the anode and cathode. To ensure even distribution of electrical current, the cathode electrodes were securely taped to the stainless-steel flow field plate using a copper frame. The electrolyzer bolts were appropriately tightened with equal compression torque. Prior to conducting the electrochemical testing, the anion exchange membrane was activated in 1 M KOH solution for more than 24 hours. Once the electrolyzer assembly was completed, the anolyte (0.5 M $KHCO_3$) flowed through the anode at a constant rate of 18 mL/min using a peristaltic pump with silicone tubing to circulate the anolyte, while the humidified CO_2 was supplied from the gas diffusion electrode (GDL) at a constant flow rate of 50 standard cubic centimeters per minute (sccm). The OER was then initiated by applying a constant current density (100, 200, and 500 mA cm^{-2}) for long term stability tests. The corresponding cell potentials for the current densities of interest were recorded with continuous monitoring. The full-cell potentials were reported without IR correction. Gas products were analyzed using GC (Agilent 6890) to determine the gas product yield. For each current density tested, the gas products were collected upon complete stabilization of the cell voltage at least three times.

Material characterization

Scanning electron microscopy (SEM) images were captured on a Hitachi S4800 with a working accelerating voltage of 10 kV. Glancing-incidence X-ray diffraction (GIXRD) was measured on a PANalytical X'Pert Pro MRD diffractometer with Cu Kα radiation (1.54 Å) at an incidence angle of 0.3°. X-ray photoelectron spectroscopy (XPS) measurements were carried out on a Thermo-VG Scientific ESCALab 250 microprobe with a monochromatic Al Kα X-ray source (1486.6 eV). The obtained spectra were calibrated using the C 1s line. The catalyst was sonicated from the carbon paper in IPA solution. Then the solvent was drop casted onto ultrathin lacey carbon TEM grids for imaging. Some residue carbon paper is hard to separate from the samples. Aberration-corrected scanning transmission electron microscopy high-angle annular dark field (AC-STEM-HAADF) images were taken on an FEI Titan 80-300 HB TEM equipped with energy-dispersive X-ray spectroscopy (EDX) at 80 kV. The HAADF-STEM images were recorded by FEI Titan 80-300 HB TEM/STEM with double aberration correctors operating at 80 kV at the Canadian Center for Electron Microscopy (CCEM). Inductively coupled plasma mass spectrometry (ICP-MS) analyses of Ru and Ir abundances were carried out on an Agilent 8800 triple quadrupole ICP-MS, using He as a collision cell gas, and In and Bi as internal standards to correct for instrument drift. Primary ICP calibration standards were from Aristar VWR Chemicals BDH. Analysis of secondary standards from Delta Scientific Inorganic Ventures confirmed instrument accuracy to within 3%. Detection limits and background equivalent concentrations were < 3 ppt (parts-per-trillion) for both Ru and Ir. Gas chromatography (GC) tests were conducted on an Agilent 6890 machine with Carboxen (TCD) and Carbonplot (FID) columns. Scanning transmission Soft X-ray microscopy (STXM) measurements were carried out at the Soft X-ray Spectromicroscopy (SM) beamline at the Canadian Light Source. XAS measurements were carried out at the 20-BM beamline of the Advanced Photon Source (APS), Argonne National Laboratory. The measurements at the Ir L-edge and Ru K-edge were performed in fluorescence mode using a Ge detector. The Ir L-edge and Ru K-edge XANES and EXAFS data were analyzed and treated using the software package Athena. The EXAFS data was fitted using the software package Artemis. Ir and Ru foil was applied for reference and calibration samples. In this fitting data, CN represents the coordination numbers of identical atoms; R is assigned as the interatomic distance; δ^2 denotes the Debye-Waller factors; and *R* factor is the goodness of fit. The fitting parameters strictly comply with all experimental requirements.

In situ Raman test

Raman spectra were conducted with a Renishaw inVia Reflex system equipped with a 100× objective and a 633 nm excitation (Renishaw HeNe laser, 17 mW). The filter was set at 5% of maximum intensity. The measurements were performed in a modified flow cell. The as-prepared catalysts, Ag/AgCl, and platinum wire were used as the working, reference, and counter electrodes, respectively. The 50 mL of 0.5M $KHCO_3$ electrolytes was continuously circulated through the flow cell during electrolysis. All applied currents were recorded without iR compensation.

In situ ATR FT-IR test

Measurements were performed at 02B1-1 Far-IR beamline of the Canadian Light Source (CLS). In situ ATR FT-IR spectra were conducted using a Bruker IFS 125 HR spectrometer with a custom-built Veemax III variable angle reflectance system (Pike Technologies, USA), and all spectra were shown as the absorbance [-log(R/R_0)]. The catalyst ink was dropped cast onto an ITO-coated SI Microgrooved Wafer Element with a 55° Face angle and dried in air before testing. A platinum wire and an Ag/AgCl electrode were used as counter and reference electrodes, respectively, in a customized electrochemical cell. The 50 mL of 0.5 M $KHCO_3$ electrolyte was continuously circulated during OER. The applied potentials ranged from 0.5V to 3V, and infrared spectra were collected every 2 min. All applied potentials were not iR corrected.

Computational details

The computational results presented in this study were performed using the Vienna Ab initio Simulation Package (VASP, version 5.4.4[27, 28]) in conjunction with the Atomic Simulation Environment (ASE) interface[29]. All spin-polarized density functional theory (DFT) calculations utilized the PBE exchange-correlation functional[30]. The electron-ion interactions were described using projector-augmented wave (PAW) potentials[31, 32].

The (110) surface of IrO_2 was employed for surface calculations. The tetragonal $P4_2/mnm$ space group bulk structure of IrO_2, was utilized from Materials Project identifier mp-2723[33]. to construct the IrO_2(110) surface. First, the lattice parameters of the bulk structure were optimized with a plane-wave cutoff of 520 eV and a Monkhorst-Pack k-point mesh of (5 × 5 × 7). Subsequently, a (1 × 2 × 4) IrO_2(110) surface was constructed based on the optimized bulk structure, with a 20Å vacuum spacing between repeating structures in the z-direction. To simulate the Ru-doped model structures, Ir atoms from the surface and subsurface layer(s) were substituted with Ru, with a total atomic percentage ranging from 6 to 19 %. The surface geometry was optimized using a plane-wave cutoff of 520 eV and a Monkhorst-Pack k-point mesh of (4 × 4 × 1). The convergence criteria for electronic and ionic iterations in geometry optimizations were set to 10^{-6} eV and 0.03 eV/Å, respectively.

The vacancy formation energy is evaluated using eq. (4):

$$\Delta E_f = E_{\text{slab + vacancy}} - (E_{\text{slab}} - 1/2\,\mu O_2) \qquad (4)$$

where, ΔE_f represents the formation energy of the oxygen vacancy, $E_{\text{slab + vacancy}}$ is the total energy of the slab model with an oxygen vacancy, E_{slab} is the total energy of the perfect slab without a vacancy, and $1/2\,\mu O_2$ is the chemical potential of oxygen expressed as $1/2E(O_2) = E_{H2O} - E_{H2}$. This approximation is commonly used to mitigate known DFT limitations in computing the total energy of gas-phase triplet O_2 and ensures consistency with prior electrocatalysis literature. While referencing H_2O directly would provide a more direct link

to electrode potential, our focus on relative stability trends justifies this widely accepted approach. The equation (4) essentially quantifies the energy required to form an oxygen vacancy. A lower formation energy indicates a more stable oxygen vacancy. If ΔE_f is negative, it implies that the formation of the oxygen vacancy is energetically favorable.

In evaluating the free energy for both gas-phase molecules and adsorbed species in each step of the OER, we considered zero-point energy (ZPE) and entropic (S) corrections obtained from a vibrational analysis performed at 298.15 K. Gas-phase molecules and adsorbed species were analyzed under the Ideal-gas oscillator limit and Harmonic limit, respectively. To approximate solvation effects, we applied the implicit solvation corrections proposed by Siahrostami and Vojvodic[34] for rutile-type oxides, which are widely accepted in modeling IrO_2-based electrocatalysts. This correction helps account for stabilization of adsorbed intermediates at the electrochemical interface in the absence of explicit solvent or continuum models. Following this analysis, the free energy change is expressed as:

$$\Delta G_i = \Delta E_i + \Delta ZPE - T\Delta S \quad (5)$$

where ΔE_i denotes the energy difference between the reactant and product.

The theoretical overpotential, denoted as η^{OER}, is defined as,

$$\eta^{OER} = \max[\Delta G_1, \Delta G_2, \Delta G_3, \Delta G_4]/e - 1.23V \quad (6)$$

By considering the difference between ΔG_{O*} and ΔG_{HO*} as a distinctive descriptor for OER activity, the theoretical overpotential (under standard conditions: T = 298.15 K, P = 1 bar, pH= 0) can be expressed as:

$$\eta^{OER} = \{\max[(\Delta G_{O*} - \Delta G_{HO*}), 3.2eV - (\Delta G_{O*} - \Delta G_{HO*})]/e\} - 1.23V \quad (7)$$

Despite being a thermodynamic quantity, this equation reliably correlates with experimentally determined overpotentials.

Results and discussion

Materials characterization of electrocatalysts

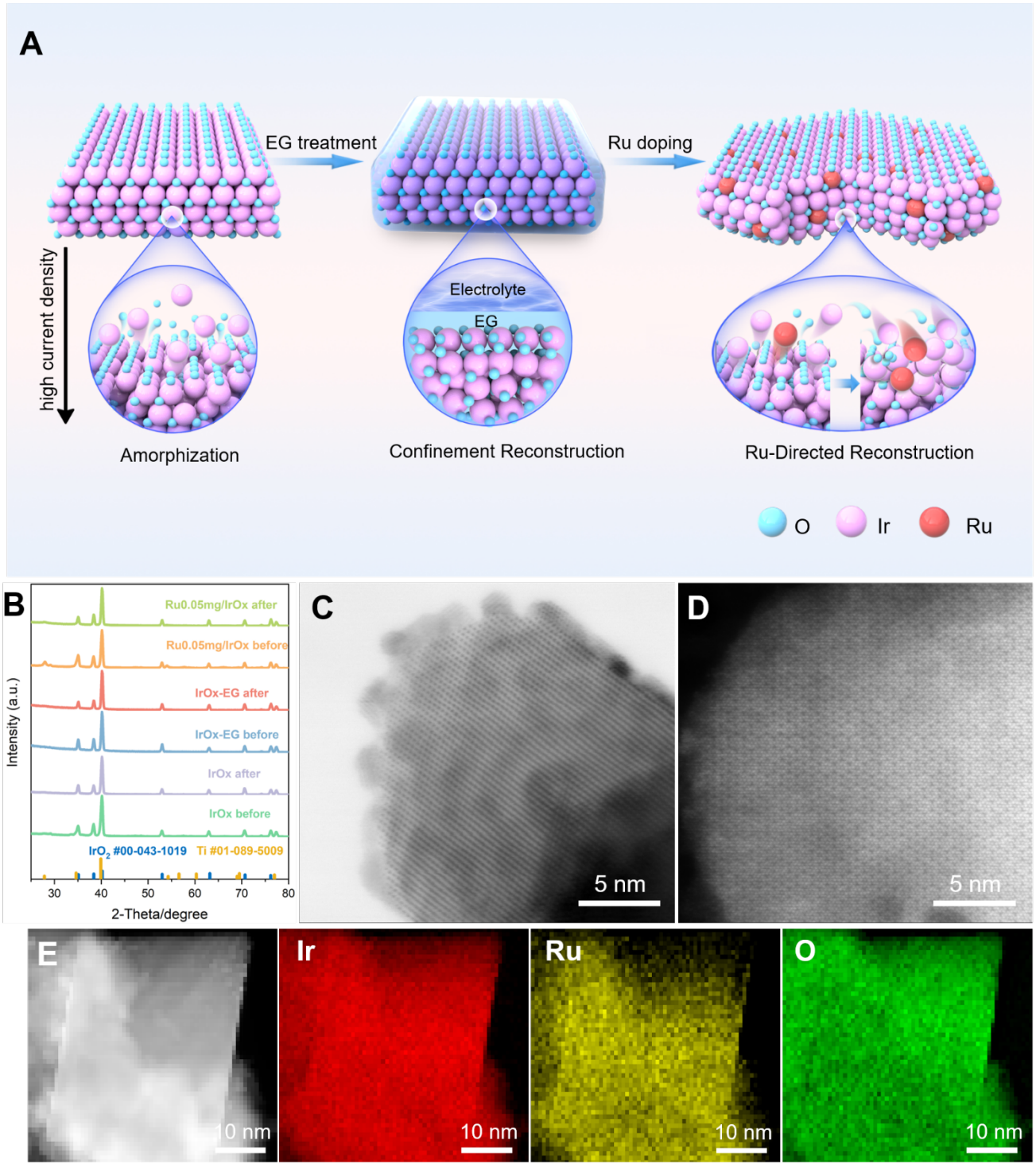

Figure 1. Synthesis and structural characterization. (A) Schematic illustration of the confinement reconstruction strategy at atomic scale. (B) GIXRD spectra of IrO_x and Ru0.05mg/IrO_x before and after the stability test under current density of 500mA cm^{-2}; (C-D) AC-HAADF-STEM images of Ru0.05mg/IrO_x before reaction (C) and after 12h stability test under current density of 500mA cm^{-2} (D); (E) EELS maps of Ru0.05mg/IrO_x after stability test with corresponding HADDF-STEM image.

We conceived a confined reconstruction strategy to reverse the formation of amorphous structures, ensuring the ordered reconstruction of IrO_x catalysts under high current densities (**Fig. 1A**). EG acts as a structural modulator, forming a protective layer-like structure on the surface, which suppresses the generation of soluble Ir species. Meanwhile, Ru functions as a stabilizing factor, promoting the dissolution-redeposition processes of IrO_x in a more ordered manner, thus enhancing the structural durability of the catalyst. The pristine IrO_x sample was synthesized via salt electrodeposition onto a Ti felt substrate, exhibiting a nanoneedle morphology (**Fig. S1A-C**). However, after a 12-h stability test at a current density of 500 mA cm^{-2}, although the morphology remained unchanged, significant catalyst dissolution occurred, leading to detachment from the substrate and a noticeable decrease in coverage (**Fig. S1D-F**). In contrast, the morphology of IrO_x-EG transformed from nanoneedles into spherical nanoparticles after the stability test, which remained tightly anchored to the substrate (**Fig. S1G-L**). This indicates that the protective layer-like structure formed by EG on the catalyst surface reduced the dissolution rate of Ir, influenced the reconstruction pathway of IrO_x particles, and prevented the formation of disordered amorphous phases. Notably, the introduction of Ru single atoms onto the IrO_x substrate resulted in a particulate morphology (**Fig. S2A-C**). After 4 h of stability testing at 500 mA cm^{-2}, the catalyst exhibited a reconstruction behavior similar to that of the IrO_x-EG sample (**Fig. S2D-F**). When the stability test duration was extended to 12 h, the catalyst remained stably adhered to the substrate, while the particle structure became increasingly refined (**Fig. S2G-I**), indicating a further progression toward an ordered reconstruction.

To investigate the structural evolution mechanism of the catalyst, we conducted a series of ex situ characterizations. Since the grazing incidence X-ray diffraction (GIXRD) patterns of all samples exhibited characteristic diffraction peaks corresponding to the rutile-phase IrO_2 (PDF card No. 43-1019) (**Fig. 1B**), it was challenging to directly observe the structural transformations in bulk phase. However, GIXRD analysis revealed that Ru single atoms did not form any distinct bulk phase (**Fig.1B**). The absence of noticeable changes in GIXRD pattern further indicated that no bulk phase transformation occurred. To further analyze the local microstructural changes of the catalyst under high current density, we employed aberration-corrected high angle angular dark field scanning transmission electron microscopy (AC-HADDF-STEM). The comparison of STEM images and EDS mapping of IrO_x before and after the stability test clearly demonstrated that catalyst underwent structural reconstruction and amorphization under high current density (**Fig. S3 vs Fig. S4**). However, after EG treatment, the post-reaction IrOx-EG sample exhibited a 4-fold symmetry [IrO_6] octahedral structure (**Fig. S5A-D, Table S1**), indicating that EG facilitated the ordered reconstruction of IrO_x, transforming it from an amorphous to a crystalline state and ultimately forming a stable rutile-like structure. The EELS mapping further demonstrated that, after reconstruction, Ir and O were homogeneously distributed within the bulk phase (**Fig. S6A-B**). Interestingly, in the Ru0.05mg/IrO_x sample, single-atom Ru doping also enhanced the crystallinity of IrO_x, leading to the formation of a stable 4-fold symmetry [IrO_4] octahedral structure revealed by the combination of AC-HADDF-STEM with extended X-ray fine structure (**Fig. 1C, Fig. S7A-D,** and **Table S1**). EELS spectroscopy revealed that Ru was uniformly distributed in the bulk phase (**Fig. S8A-B**), suggesting that Ru, as a single-atom dopant, was homogeneously and stably incorporated into the IrO_x structure. After a 500 mA cm^{-2} stability test, the

catalyst underwent an ordered structural transformation from original 4-fold symmetry [IrO_4] to a 6-fold [IrO_6] octahedral structure revealed by the combination of AC-HADDF-STEM with extended X-ray fine structure (**Fig. 1C-D, Fig. S9A-D,** and **Table S1**). This observation indicates that Ru single-atom doping serves as a structural stabilizing factor, promoting a high degree of crystallization. Although it is difficult to distinguish the Ru atomic position from Ir by Z-contrast direct imaging due to the close atomic numbers, the EELS mapping confirmed that Ir, Ru, and O remained homogeneously distributed within the bulk phase (**Fig. 1E** and **Fig. S10**), indicating ordered reconstruction under high current density conditions.

X-ray photoelectron spectroscopy (XPS) was employed to analyze the surface composition and chemical states of the catalysts. In all pre- and post-reaction samples, the Ir 4f spectra could be deconvoluted into two distinct peaks, corresponding to Ir^{3+} and Ir^{4+} oxidation states (**Fig. S11A**)[13, 35], while the O 1s spectra exhibited three components, attributed to lattice oxygen, adsorbed hydroxyl species, and molecularly adsorbed water (H_2O) (**Fig. S11B**)[36, 37]. A comparative analysis of the elemental compositions obtained from XPS fitting revealed that, after the stability test, the Ir^{4+} content in the Ru0.05mg/IrO_x sample increased significantly (**Fig. S11C**). This could be attributed to the partial oxidation of surface Ir atoms in Ru0.05mg/IrO_x, likely caused by the adsorption of surface hydroxyl species or the accumulation of oxygenated intermediates under OER conditions, resulting in an apparently higher Ir^{4+} ratio. However, the proportion of lattice oxygen decreased markedly compared to IrO_x and IrO_x-EG (**Fig. S11D**), indicating that Ru doping facilitated the ordered reconstruction of the IrO_x lattice, thus enhancing structural stability and mitigating the detrimental effects of lattice oxygen. To identify possible organic species on the catalyst surface, C 1s XPS analyses were performed on IrO_x, IrO_x–EG, and Ru0.05mg/IrO_x catalysts before and after the reaction. For the IrO_x catalyst synthesized using water as the solvent, no organic species were detected on the surface (**Figure S11E**). In contrast, both IrO_x–EG and Ru0.05mg/IrOx catalysts exhibited similar organic species before and after the reaction (**Figure S11E**), indicating the stable presence of the EG protective layer throughout the electrochemical process. The oxygen K-edge X-ray absorption spectroscopy (XAS) spectra were acquired using synchrotron-based scanning transmission X-ray microscopy (STXM) (**Fig. 2A**). Notably, while XPS confirmed the presence of Ir^{4+}, STXM XAS did not exhibit a corresponding spectral feature, suggesting that Ir^{4+} was primarily located on the catalyst surface or that the Ir valence edges (M and N edges) exhibited low sensitivity in STXM measurements. Oxygen K-edge XAS probed the electronic transition from oxygen 1s orbitals to unoccupied states derived from the hybridization between oxygen 2p and metal d orbitals. Thus, these spectra provided insight into the covalency of the metal-oxygen bonds. Changes in the intensity of peaks 1, 2, and 3 indicated an enhanced Ir–O covalency in Ru0.05mg/IrO_x after the reaction, relative to its state before the reaction (**Fig. 2A**). The increased Ir–O covalency in Ru/IrO_x suggested a reduction in the number of unoccupied Ir 5d orbitals, implying a decrease in the Ir oxidation state in Ru0.05mg/IrO_x after the reaction. In contrast, IrO_x exhibited lower Ir–O covalency (**Fig. 2A**), indicating a higher population of unoccupied Ir 5d orbitals and thus a higher Ir oxidation state after the reaction, suggesting the generation of soluble Ir species. This contrast in Ir–O covalency may be attributed to a Ru-induced structural reconfiguration mechanism during the OER that did not occur in undoped IrO_x. Additionally, Ru incorporation as single atoms enhanced the stability

of the IrO_x structure, mitigating lattice distortion and suppressing the formation of undercoordinated Ir sites, which were prone to dissolution. This Ru-stabilized IrO_x framework contributed to improved long-term durability during OER. The oxygen K-edge spectra of both Ru0.05mg/IrO_x and IrO_x exhibited distinct features from commercial IrO_2 (**Fig. 2A**), further suggesting the presence of oxygen vacancies in both materials, which may contribute to the catalytic activity. Moreover, while STXM XAS did not show evidence of RuO_2 formation, extended X-ray absorption fine structure (EXAFS) analysis confirmed Ru–O bonding (**Table S2**), indicating the presence of Ru in an oxidized state. This discrepancy could be attributed to the low sensitivity of O K-edge XAS for detecting RuO_2 at low doping concentrations.

To further investigate the evolution of the chemical state and local coordination environment of the catalyst before and after the reaction, we conducted Ir L_3-edge and Ru K-edge XAS measurements. Under OER conditions, the Ir L_3-edge XANES spectra of IrO_x exhibited a shift toward higher energy (**Fig. 2B**), indicating that IrO_x underwent partial dissolution during electrochemical reconstruction, potentially transforming into a more amorphous or higher oxidation state, leading to a shortening of the Ir–O bond length (**Fig. 2C, Fig. S12A-H, and Table S1**). During this reconstruction, the local coordination environment of Ir was partially disrupted, leading to a reduction of the Ir–Ir coordination number and an elongation of the Ir–Ir bond length (**Table S1**). However, after EG treatment, the Ir L_3-edge XANES spectra of IrO_x-EG (before vs after reaction) did not show a significant shift to higher energy as observed in the pristine IrO_x after OER (**Fig. 2B**), suggesting that EG effectively regulated the oxidation state of Ir, suppressing Ir overoxidation and reducing the formation of soluble Ir species. During OER, IrO_x-EG did not undergo severe amorphization but rather tended to form a distorted [IrO_6] octahedral structure, where the Ir–O coordination number (5.8) was close to 6, and the Ir–O bond length was 1.99 Å (**Fig. 2C** and **Table S1**). Additionally, the Ir–Ir coordination number did not significantly decrease as observed in pristine IrO_x but remains at 3.1 (**Table S1**), indicating that IrO_x-EG retained a certain degree of long-range order after structural reconstruction. Meanwhile, the Ir–Ir bond length remained at 3.24 Å (**Table S1**), which was close to the standard IrO_2 lattice parameter. In the Ru0.05mg/IrO_x system, before the reaction, the absorption edge of Ir closely aligned with that of IrO_2 references, whereas Ru exhibited a noticeably higher oxidation state than RuO_2 reference (**Fig. 2B** and **D**). This could be attributed to the fact that the strong electronic coupling between Ru and the surrounding Ir–O matrix induced charge redistribution, leading to a partially oxidized Ru center with a higher oxidation state and coordination number than RuO_2 reference (**Table S2**). EXAFS fitting results clearly showed the absence of Ru–Ru coordination and the presence of only Ru–O bond (**Fig. 2E** and **Table S2**), confirming the single-atom nature of Ru. Ir primarily presented in a four-coordinated Ir–O configuration (**Table S1**), and Ru single atoms mainly occupied low-coordination sites on the IrO_x surface ([RuO_4], Ru–O_{CN} = 4) (**Fig. 2E, Fig. S13,** and **Table S2**). During long-term OER operation under high current density, an interaction between Ru and IrO_x occurred, ultimately forming a more stable octahedral coordination structure. In this process, Ir gradually transitioned into a nearly ideal [IrO_6] octahedral configuration (Ir–O_{CN} = 6) (**Table S1**), while Ru underwent a transformation from 4-fold [RuO_4] to 6-fold symmetry, eventually forming a [RuO_6] octahedral structure (Ru–O_{CN} = 6) (**Table S2**).

This transition was likely influenced by the presence of surrounding oxygen species (*O, *OH), which facilitated the rearrangement of Ru coordination, leading to its incorporation into the IrO_x lattice and the formation of a stable Ru–O–Ir interconnected structure, thereby significantly enhancing the catalyst's durability. In the six-fold symmetric structure, the coordination between Ru and Ir was more compact, contributing to the stabilization of active reaction sites. Moreover, the single-atom Ru was likely in a relatively stable state, where its strong interaction with Ir and O atoms ensured minimal structural variations in the catalyst. The stability of single-atom Ru played a crucial role in maintaining the overall stability of the catalyst, particularly under high current densities. To further verify the local coordination environment of Ir and Ru, we conducted wavelet transform (WT) analysis. Compared to IrO_2 reference (**Fig. 2F**), Ir foil, and IrO_x (**Fig. S14A-C**), IrO_x-EG predominantly maintained an Ir–O coordination environment, preserving a high degree of structural stability (**Fig. S14D-E**). More importantly, in the Ru0.05mg/IrO_x system, Ir transitioned from Ir–Ir coordination to Ir–O coordination (**Fig. S14F** vs **Fig. 2G**), while Ru remained in the Ru–O coordination form before and after the reaction (**Fig. S14G-H** vs **Fig. 2H-I**, **Table S2**), further confirming the formation of a Ru–O–Ir interconnected structure, which provided crucial evidence for the high stability of the catalyst under OER conditions.

In ICP-MS analysis, the change in catalyst loading can be used to evaluate the structural stability of the catalyst during the reconstruction process **(Table S3**). For the IrO_x catalyst, the loading amount significantly decreased after the stability test, indicating the formation of a large number of soluble species **(Table S3**). This also demonstrated the instability of IrO_x under high current densities, which tended to undergo amorphization. In contrast, after introducing the EG protective layer, the formation of soluble species during the reconstruction process was effectively suppressed **(Table S3**). Furthermore, the Ru single-atom doping induced an ordered reconstruction of the catalyst, forming a more stable high-coordination [IrO_6] and [RuO_6] octahedral structure (**Fig. 1D, Table S1-2**). Therefore, the Ru0.05mg/IrO_x catalyst showed no obvious change in loading before and after the reaction **(Table S3**).

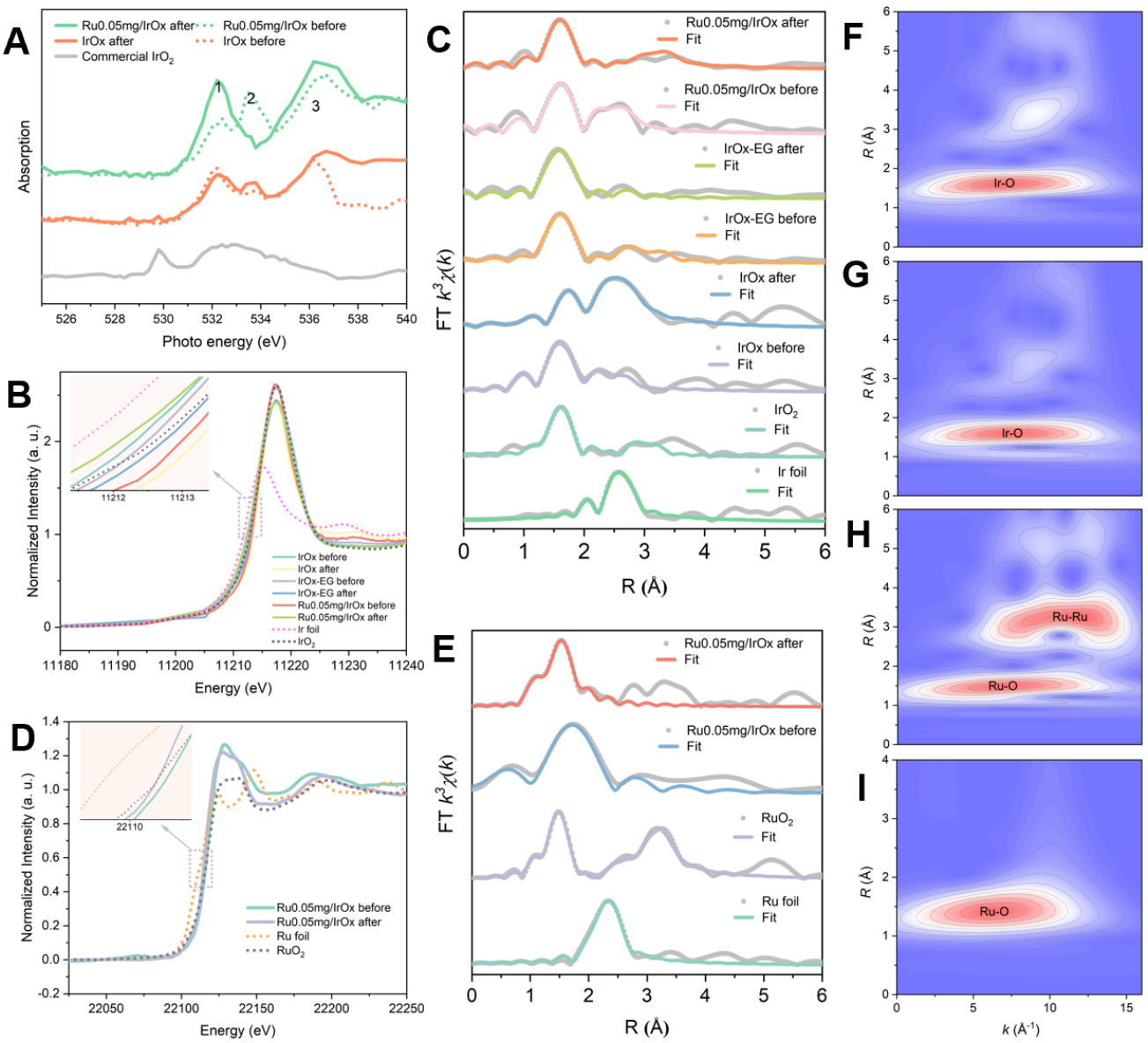

Figure 2. **Multimodal X-ray spectroscopic analysis of electrocatalysts**. (A) O K-edge x-ray absorption spectra of Ru0.05mg/IrO_x and IrO_x before and after reaction. (B) Ir L_3-edge XANES spectra of as-prepared samples before and after reaction and corresponding references (Ir foil and IrO_2). (C) Ir L_3-edge Fourier-transform EXAFS spectra of as-prepared catalysts and corresponding references (Ir foil and IrO_2); (D) Ru K-edge XANES spectra of Ru0.05mg/IrO_x samples before and after reaction and corresponding references (Ru foil and RuO_2). (E) Ru K-edge Fourier-transform EXAFS spectra of Ru0.05mg/IrO_x catalysts and corresponding references (Ru foil and RuO_2). (F-G) Wavelet transforms for k^3-weighted EXAFS signals of Ir L_3-edge of IrO_2 (F) and Ru0.05mg/IrO_x after reaction (G). (H-I) Wavelet transforms for k^3-weighted EXAFS signals of Ru K-edge of RuO_2 (H) and Ru0.05mg/IrO_x after reaction (I).

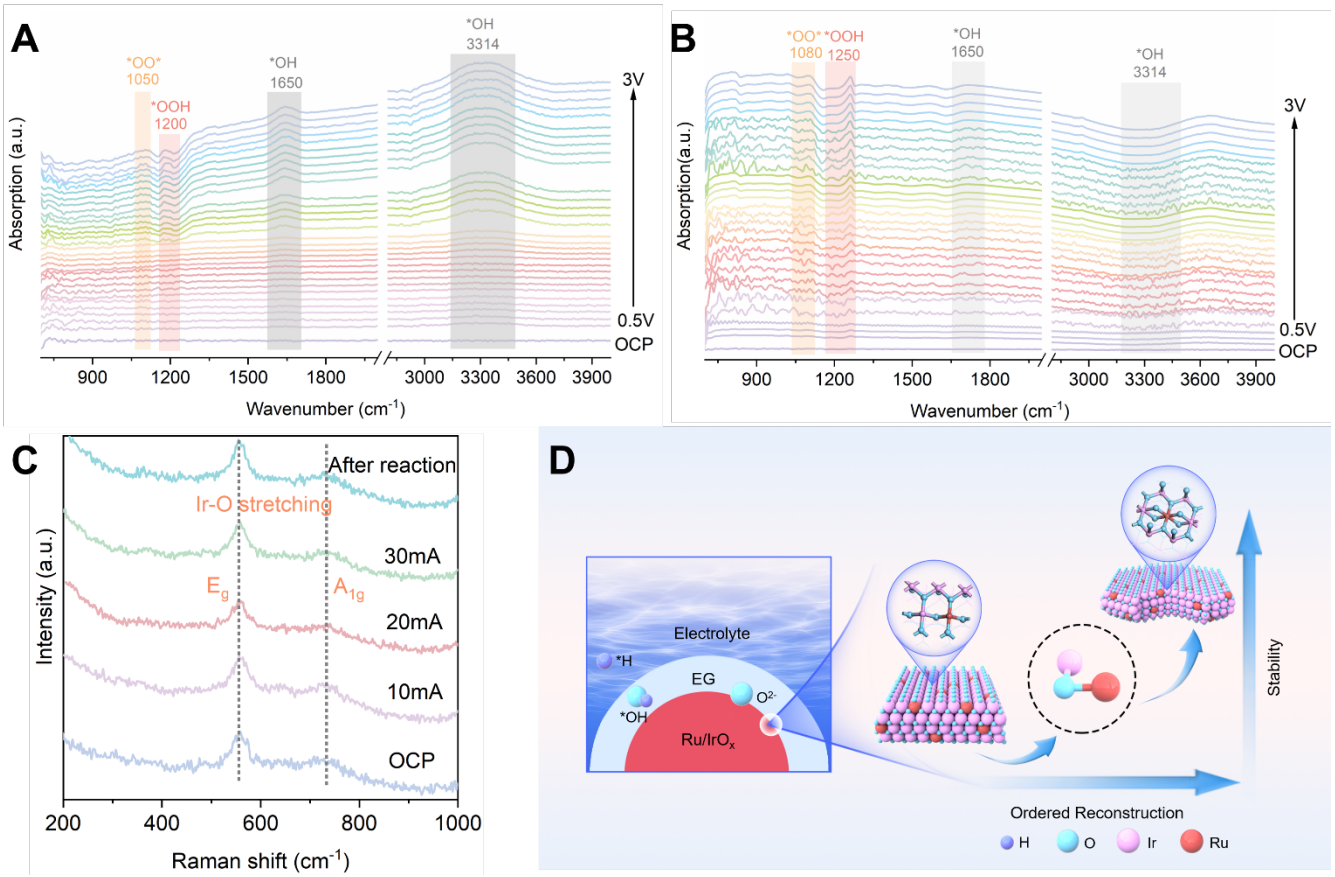

Figure 3. (A-B) In situ real-time ATR FT-IR spectra of the Ru0.05mg/IrO_x (A) and IrO_x (B) catalysts were recorded under various applied potentials in 0.5M $KHCO_3$ electrolyte. (C) In situ Raman test of Ru0.05mg/IrO_x using 0.5M $KHCO_3$ electrolytes under various currents. All applied potentials and currents were not iR corrected. (D) The proposed mechanism diagram of the ordered reconstruction.

To monitor the evolution of surface-adsorbed intermediates during the reaction, in situ attenuated total reflection Fourier-transform infrared (ATR-FTIR) spectroscopy was employed. For Ru0.05mg/IrO_x (**Fig. 3A** and **Fig. S15**), as the potentials increased, absorption bands at 3314 cm^{-1} and 1650 cm^{-1} progressively intensified and then stabilized[38]. These bands are attributed to the stretching and bending vibrations of hydrogen-bonded hydroxyl groups, respectively, indicating adsorption of H_2O molecules on the catalyst surface and the onset of the OER. Once the potential exceeded 1.4 V, the emergence of the *OO* intermediate at 1050 cm^{-1} indicated that the catalyst followed the oxide path mechanism (OPM)[39], implying the formation of oxygen bridge structures at the catalytic sites. Furthermore, the appearance of the *OOH intermediate at 1200 cm^{-1}[40] suggests that the catalytic process more closely aligned with the adsorbate evolution mechanism (AEM), rather than the conventional OPM or lattice-oxygen-mediated mechanism (LOM). Notably, no *OO* or *OOH intermediate bands were observed at potentials below 1.5 V (**Fig. S15A-B**), indicating that structural reconstruction of the catalyst did not occur at low current densities and that only H_2O adsorption was initiated under these conditions. Importantly, even after the

external potential was removed, all key adsorption bands remained stable (**Fig. S15A-E**), confirming that Ru0.05mg/IrO_x underwent an irreversible and ordered reconstruction under high current densities. For IrO_x, the *OH, *OO*, and *OOH adsorption bands were also observed, indicating that IrO_x followed a similar reaction mechanism (**Fig. 3B**). Such reconstruction behavior involved the oxygen-bridge formation seen in OPM-type mechanisms but ultimately follows the AEM pathway, favoring the stable generation of *OOH species and efficient O_2 evolution. However, the stability of active sites within the oxygen-bridge structures cannot be directly verified by in situ ATR-FTIR. Therefore, in situ Raman spectroscopy was employed to further reveal the evolution of the surface structure. For the Ru0.05mg/IrO_x catalyst, the Ir–O stretching mode remained at the same position and showed excellent stability with increasing current[10] (**Fig. 3C**), indicating a robust Ir–O structure. In contrast, for pristine IrO_x, although the Ir–O stretching mode was observable at low currents, it gradually disappeared at higher current densities (**Fig. S16**), suggesting amorphization of the catalyst structure. These results confirmed that Ru single-atom doping and the EG protective layer effectively enhanced the stability of the Ir–O–Ru bridging structure and promote an ordered reconstruction during OER operation.

Based on these results, we proposed a plausible reconstruction mechanism at high current densities (**Fig. 3D**). EG contained hydroxyl groups that could chelate with surface Ir atoms, modulating the local coordination environment and promoting controlled nucleation during electrochemical activation. It not only suppressed the over-oxidation of Ir species into soluble forms, preventing amorphization, but also ensured the stability of Ir–O bonds, thereby promoting an ordered reconstruction process (**Fig. S5-6**). During the initial stage of the OER, Ru existed predominantly in a high oxidation state (**Fig. 2D**) and preferentially adopted a lower coordination number (**Table S2**) to accommodate its electronic configuration. Consequently, it anchored onto the IrO_x framework in a four-coordinated [RuO_4] structure (**Table S2**). However, as the OER progressed, the high anodic potential promoted the accumulation of oxygen intermediates (*OO, *OOH, *OH) (**Fig. 3A-B** and **Fig. S15**). Direct O*–O* coupling occurred between adjacent Ru and Ir sites, leading to the formation of oxygen-bridged structures. To adapt to the evolving reaction environment, IrO_x dynamically adjusted its oxygen coordination number (**Table S1**), while high-valence Ru (**Fig. 2D**) exhibited increased mobility, which may lead to dissolution and leaching from the bulk phase. However, under the protective effect of EG, an ordered reconstruction process was triggered, where Ru gradually integrated into the IrO_x lattice through the formation of robust Ru–O–Ir bridging structures. This process stabilized Ru within the IrO_x framework, enabling a progressive transition from a four-coordinated to a six-coordinated oxygen environment. The final [RuO_6]/[IrO_6] octahedral configuration (**Table S1, Table S2**) enhanced the structural rigidity of the catalyst and significantly improved its long-term stability under high current density.

Electrocatalytic OER performance

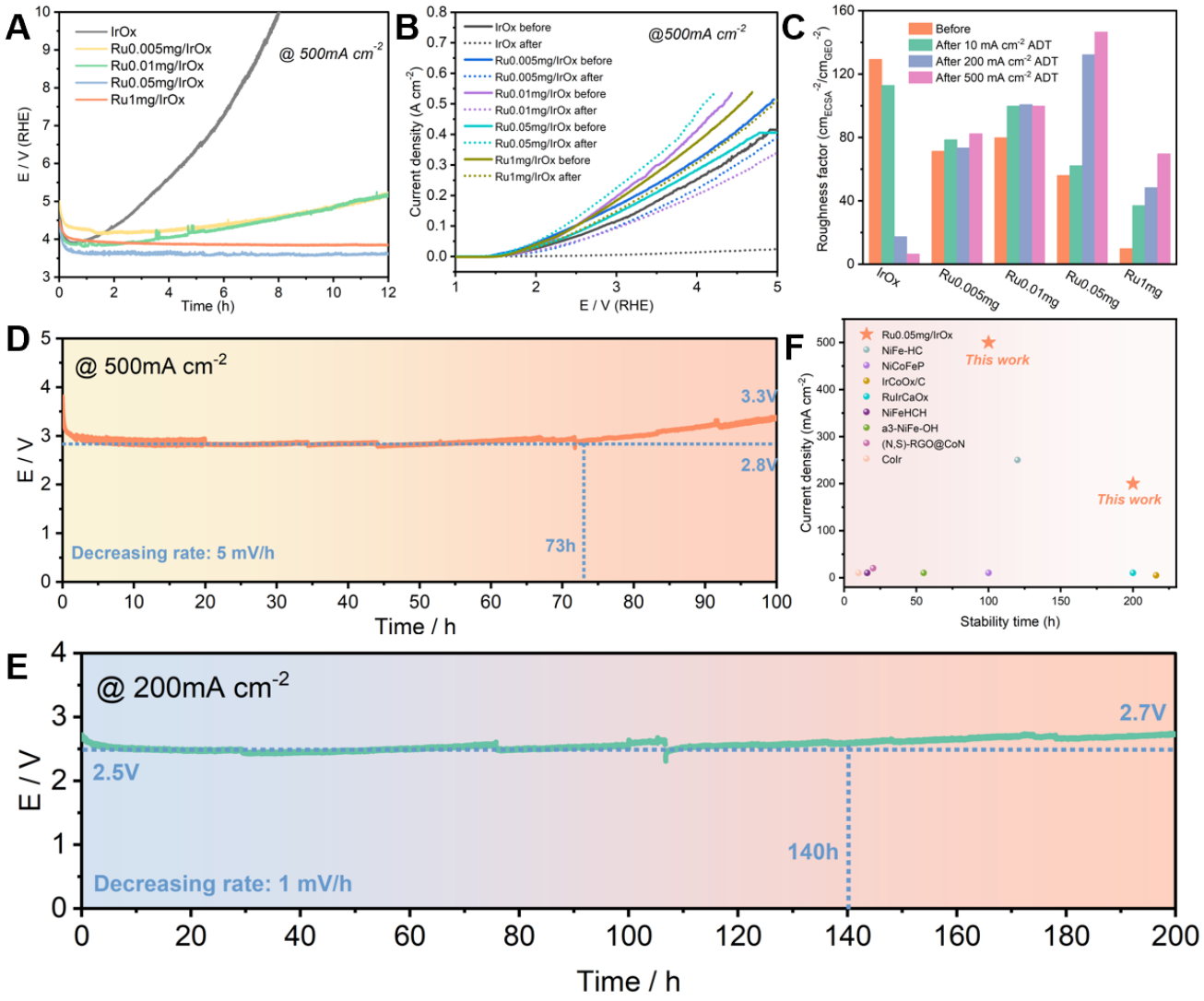

Figure 4. **OER performance and stability under neutral condition**. (A) The 12-hour stability test for IrO_x and Ru/IrO_x with varying Ru loadings at 500 mA cm^{-2}; (B) LSV curves, normalized to the geometric area, for samples with different Ru loadings before and after the 12-hour stability test at 500 mA cm^{-2}; (C) ECSA analysis comparing Ru/IrO_x with varying Ru loadings to IrO_x. (D-E) The long-term stability test of $Ru0.05mg/IrO_x$ at current densities of 500 (D) and 200 mA cm^{-2} (E). The $Ru0.05\ mg/IrO_x$ catalysts used in Figures 4D–E were subjected to 12 h of stability testing at 500 mA cm^{-2}. (F) Comparison of OER performance between $Ru0.05mg/IrO_x$ and other reported materials at neutral conditions.

To evaluate the catalytic OER performance, electrochemical measurements were conducted in a three-electrode system using 0.5 M $KHCO_3$ electrolyte. Stability tests revealed that IrO_x exhibited significant degradation at high current densities (**Fig. S17A**), with a substantial decline in OER activity after reaction (**Fig. S17B**). This suggested that IrO_x underwent dissolution and reconstruction under high-current conditions, leading to severe

performance deterioration. Notably, IrO_x-EG demonstrated significantly enhanced stability under high-current conditions (**Fig. S18A**). Moreover, after stability testing at different current densities, the IrO_x-EG exhibited improved OER activity compared to original IrO_x (**Fig. S18B vs Fig. S17B**), indicating that EG effectively inhibited IrO_x dissolution and enhances structural stability. To further optimize OER performance, Ru was incorporated into the catalyst, and various Ru/Ir ratios were investigated. Prior to stability testing, LSV results showed that Ru doping enhanced the OER activity, with the optimal performance observed at a Ru0.01 mg/IrO_x (**Fig. S19**). The 12-h stability testing indicated that at low current densities, all samples maintained good stability at 10 and 200 mA cm^{-2} (**Fig. S20A-B**). However, under a high current density of 500 mA cm^{-2}, only catalysts with Ru loadings of 0.05 mg and 1 mg exhibited superior durability (**Fig. 4A**). Furthermore, post-reaction OER performance analysis revealed that, except for Ru0.05mg/IrO_x, which exhibited an anomalous increase in activity, all other samples suffered performance degradation (**Fig. 4B** and **Fig. S21A-H**). This suggested that an appropriate amount of Ru doping not only enhanced structural stability but also improved catalytic activity. Notably, at low current densities, Ru1mg/IrO_x exhibited the highest OER activity (**Fig. S22A**), whereas at high current densities, Ru0.05mg/IrO_x demonstrated superior catalytic performance (**Fig. S22B-C**). This indicated that under low current density conditions, the catalyst retained its original 4-fold symmetry [IrO_4] and [RuO_4] octahedral-like structure as the primary active site (**Table S1**). However, at high current densities, an appropriate amount of Ru acted as a structural stabilizing factor, facilitating catalyst reconstruction to form 6-fold symmetry [IrO_6] and [RuO_6] octahedral structures (**Table S1, Table S2**), thereby further enhancing catalytic activity and stability. This observation underscored the structural advantages introduced by appropriate Ru doping. To elucidate the origin of the enhanced catalytic activity, electrochemical double-layer capacitance (C_{dl}) measurements were employed to estimate the electrochemically active surface area (ECSA) of catalysts (**Fig. S23-28**). In the ECSA-normalized activity comparison, the activity ranking remained largely unchanged before and after the stability test, with Ru1mg/IrO_x consistently exhibiting the highest intrinsic activity (**Fig. S29A-D**). Although variations in stability and catalytic activity may be related to ECSA, it remained unclear whether ECSA was the sole determining factor. Further analysis of the catalyst roughness factor revealed that under high current densities, Ru0.05mg/IrO_x exhibited the highest roughness factor, while Ru1mg/IrO_x had the lowest (**Fig. 4C**). This finding indicated that ECSA alone cannot fully account for the observed differences in catalytic performance, and additional factors such as active site exposure and structural evolution likely contribute to the enhanced OER activity of Ru0.05mg/IrO_x at high current densities.

Based on the above findings, Ru0.05mg/IrO_x was selected for long-term stability testing. Under high current densities of 500 and 200 mA cm^{-2}, the catalyst exhibited stable operation for 100 h (**Fig. 4D**) and 200 h (**Fig. 4E**), respectively. This durability significantly exceeds previously reported OER stability in neutral conditions (**Fig. 4F, Table S4**), demonstrating its promising potential for practical applications.

OER performance of electrocatalyst in a MEA-based CO_2 electrolysis

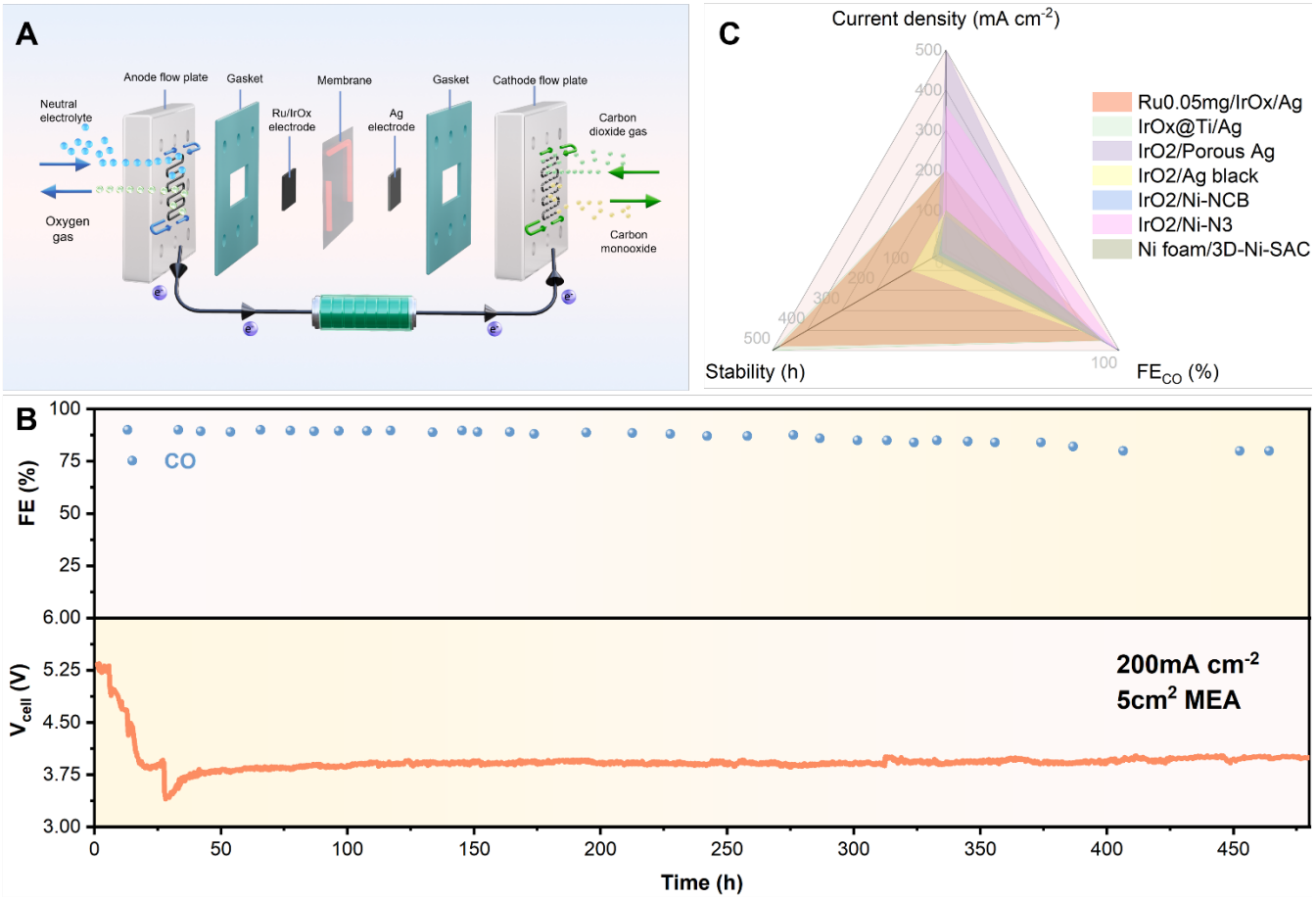

Figure 5. **eCO₂RR stability in an 5cm² MEA**. (A) A schematic illustration of the MEA electrolyzer. (B) The eCO₂RR stability test of fresh Ru0.05mg/IrO$_x$@Ag NPs at current density of 200 mA cm^{-2} using 0.5M KHCO₃. (C) Comparison of the long-term operational stability of Ru0.05mg/IrO$_x$@Ag NPs in a neutral CO_2 electrolysis using MEA reactor for CO production with other reported systems.

In the industrial application of eCO₂RR, achieving high current densities exceeding 200 mA cm^{-2} is a critical requirement. Given that the Ru0.05mg/IrO$_x$ catalyst demonstrated exceptional stability at 200 mA cm^{-2} in a conventional three-electrode configuration, we further evaluated its long-term performance in a MEA system to assess its practical viability for CO_2 electrolysis (**Fig. 5A**). The MEA device utilized a 5 cm² geometric electrode area, with Ru0.05mg/IrO$_x$ serving as the anodic catalyst for the OER and Ag nanoparticles as the cathodic catalyst for eCO₂RR, selectively producing CO. During the initial stage of electrolysis, structural instability of the catalyst led to reconstruction under high current density, causing fluctuations in cell voltage (**Fig. 5B**). However, once a stable catalytic structure was established, the MEA system maintained stable operation for 480 h (**Fig. 5B**). Over this extended period, the Faradaic efficiency (FE) of CO production gradually declined from an initial 90% to approximately 80% (**Fig. 5B**), indicating gradual but controlled catalyst degradation while preserving high selectivity. For comparison, stability tests under acidic conditions were conducted. The catalyst exhibited stable

operation for 16 h, maintaining a CO selectivity of approximately 65% with a cell voltage around 4.5V (**Fig. S30**). This result further demonstrates that eCO_2RR in a neutral electrolyte offers lower cell voltage, better stability than acid condition for industrial application. Notably, the durability of our MEA system significantly outperforms previously reported neutral-electrolyte MEA systems for CO production (**Fig. 5C, Table S5**), highlighting the structural and electrochemical advantages of the Ru0.05mg/IrO_x catalyst. The superior stability of our system was likely attributed to the synergy between Ru and Ir by confined reconstruction, where Ru incorporation promoted the formation of a high-coordination [RuO_6]/[IrO_6] octahedral framework, enhancing both intrinsic catalytic activity and resistance to dissolution. These findings underscored the strong potential of our catalyst and MEA configuration for industrial-scale eCO_2RR applications, offering a promising route toward scalable and energy-efficient CO_2 conversion technology.

Computational Results and Discussion

To better understand the reasons behind high activity and stability of Ru0.05mg/IrO_x samples in our experimental section, we utilized DFT calculations. Our integrated analysis of EXAFS (**Fig. 2E, 2I, Table S2**) and AC-HAADF-STEM images (**Fig. 1C-D**) confirms the single-atom dispersion of Ru atoms with localized coordination within the Ru/IrO_{2-x} structure. Therefore, to capture the influence of coordination environment, we constructed various model structures by incorporating different numbers of Ru single atoms doped into the IrO_{2-x} (110) rutile crystal structure (**Fig. 6A**).

The studied model structures include various content of atomic percentages of Ru, including 6%, 13% and 19%. Of note, the percentages in our computational models may not directly mirror the experimental compositions. However, constructing a variety of models for atomic configurations aids in elucidating the potential coordination chemistry that impacts the stability and activity of Ru_x-IrO_{2-x}. $Ru_{6\%}$-IrO_2 includes one Ru single atom in the IrO_2 slab, while $Ru_{13\%}$-IrO_2 and $Ru_{19\%}$-IrO_2 include two and three Ru single atoms in the IrO_2 slab, respectively. For $Ru_{6\%}$-IrO_2, we investigated three probable sites for Ru atoms, indicated as $Ru_{6\%(a)}$-IrO_2 and $Ru_{6\%(b)}$-IrO_2 and $Ru_{6\%(c)}$-IrO_2 in **Fig. 6A**, each of which corresponds to a different location for the doped Ru atom, either on the surface or subsurface of the IrO_2 slab. Specifically, in $Ru_{6\%(a)}$-IrO_2, the Ru atom is a sublayer atom located below the Ir atom active site. In $Ru_{6\%(b)}$-IrO_2, the Ru atom is a surface atom located next to the Ir atom active site. In $Ru_{6\%(c)}$-IrO_2, the Ru atom is a surface atom, and it serves as the active site.

For $Ru_{13\%}$-IrO_2, we examined two different model structures where ($Ru_{13\%(a)}$-IrO_2 and $Ru_{13\%(b)}$-IrO_2) correspond to different arrangements of Ru atoms within the IrO_2 slab. In $Ru_{13\%(a)}$-IrO_2, one Ru atom is a surface atom located next to the Ir atom active site, while another Ru atom is a sublayer atom positioned below the Ir atom active site. In $Ru_{13\%(b)}$-IrO_2, one Ru atom is a sublayer atom below the Ir atom active site, and another Ru atom is a sublayer atom next to this Ru sublayer atom. For $Ru_{19\%}$-IrO_2, we examined only one possibility due to the configuration it presents. In this structure, the two Ru atoms on the surface and the Ru atom in the sublayer are the nearest neighbor atoms to Ir at the surface for this amount of Ru.

According to our XPS findings depicted in **Fig. S11**, Ru0.05mg/IrO_x sample with reduced lattice oxygen content after OER exhibits greater stability. The rise in lattice oxygen content correlates directly with an increase in oxygen vacancies. Consequently, it is apparent that samples like IrO_2, which display a substantial increase in lattice oxygen content following OER testing, have undergone the formation of numerous oxygen vacancies, resulting in low OER stability. To investigate the stability in more detail, we calculated the formation energy of an oxygen vacancy (ΔE_f) in various model structures constructed for Ru_x-IrO_{2-x} in **Fig. 6A** using DFT calculations (see computational details in **Methods**) (**Fig. 6B**). We then compared these with the vacancy formation energy of pristine IrO_2.

The tendency of the catalyst to form an oxygen vacancy (less formation energy) is an indication of a less stable structure. The stability of IrO_2 is sensitive to different incorporations of Ru (**Fig. 6B**). IrO_2 has a negative oxygen vacancy formation energy of ΔE_f = -0.27 eV, indicating a facile loss of oxygen from site 1 (**Fig. 6B**). However, any amount of Ru incorporated into IrO_2 shifts the oxygen vacancy formation energies toward more positive values ranging from 0.1 to 0.39 eV when a vacancy is formed in site 1 (**Fig. 6B**). When subsurface oxygen vacancies are considered in Ru_x/IrO_2 structures, the oxygen vacancy formation energy is decreased indicating more tendency to form subsurface oxygen vacancies. The fact that incorporating any amount of Ru (Ru_x/IrO_2) shifts the oxygen vacancy formation energy towards more positive values indicates higher stability for Ru_x/IrO_2 structures, leading to less leaching of the Ir^{4+} into the solution during the OER in comparison with pure IrO_2. This analysis offers valuable insights into understanding the interactions between Ru dopants and IrO_2 at different crystallographic sites, leading to tailoring the IrO_2 catalytic properties toward better OER performance.

As stated earlier, it is established that catalysts operating under LOM exhibit superior activity, but inferior stability compared to those operating under AEM[27, 28]. Previous experimental and computational studies on IrO_2 and RuO_2 catalysts have demonstrated the LOM as a likely pathway for OER.[29, 30] To understand how the OER activity changes across different Ru_x/IrO_{2-x} model structures, we investigated both AEM and LOM mechanisms. We first did the analysis for the AEM mechanism[31] and calculated the adsorption free energies of OER intermediates, ΔG_{HO*}, ΔG_{O*}, and ΔG_{HOO*}. Computational hydrogen electrode (CHE) in conjunction with descriptor-based analysis was used to identify trends in OER activity across different model structures in **Fig. 6A**. The free energy difference of the key intermediates ΔG_{HO*} and ΔG_{O*} is used as the OER activity descriptor. Theoretical overpotential was calculated for all different model structures (see the computational details in **Methods**) which allowed us to establish the OER activity volcano plot (**Fig. 6C**).

The color bar in **Fig. 6C** shows the theoretical overpotential with the most active catalyst located in the red region where overpotential is minimized. Different examined structures were studied to draw the catalytic activity trends (**Fig. 6A**). Our findings reveal that Ir remains the most active site in all Ru_x/IrO_{2-x} structures. When a surface Ru atom is considered as the active OER catalytic site ($Ru_{6\%(c)}/IrO_2$) in any of the structures studied, the calculated overpotential is exceptionally high, reaching 0.71 V (**Fig. 6D**). The results in **Fig. 6C-D** indicate that even minimal percentage of Ru atoms (e.g. $Ru_{6\%(b)}/IrO_2$) modifies the electronic structure of the adjacent Ir sites,

lowering the OER overpotential and thereby increasing activity. Among the studied systems, $Ru_{13\%(a)}/IrO_2$ structure displays the least overpotential (0.38 V, **Fig. 6C-D**). In this configuration, Ru single atoms are dispersed across both the surface and the sublayer (as depicted in **Fig. 6A**), thereby altering the electronic structure of the adjacent Ir atom, which acts as an active site.

We further investigated the LOM mechanism on our most active catalyst surface, i.e., $Ru_{13\%(a)}/IrO_2$ (**Fig. 6E-F**). Our results show that the reaction mechanism may involve a combination of both LOM and AEM, with LOM potentially playing a role in initiating the reaction by facilitating the transfer of lattice oxygen atoms, which then proceed to participate in adsorbate evolution on the catalyst surface. **Fig. 6E-F** display the OER free energy diagrams on IrO_2 and $Ru_{13\%(a)}/IrO_2$ at U = 0.0 V and U = 1.23 V, considering both AEM and LOM mechanisms. LOM relies on the participation of lattice oxygen atoms, whereas AEM involves the adsorption and evolution of reactive OER intermediates on the catalyst surface. Thus, we further calculated the adsorption energy of the key intermediate steps for LOM, ΔG_{HO*}, ΔG_{2HO*}, and ΔG_{2O*}.

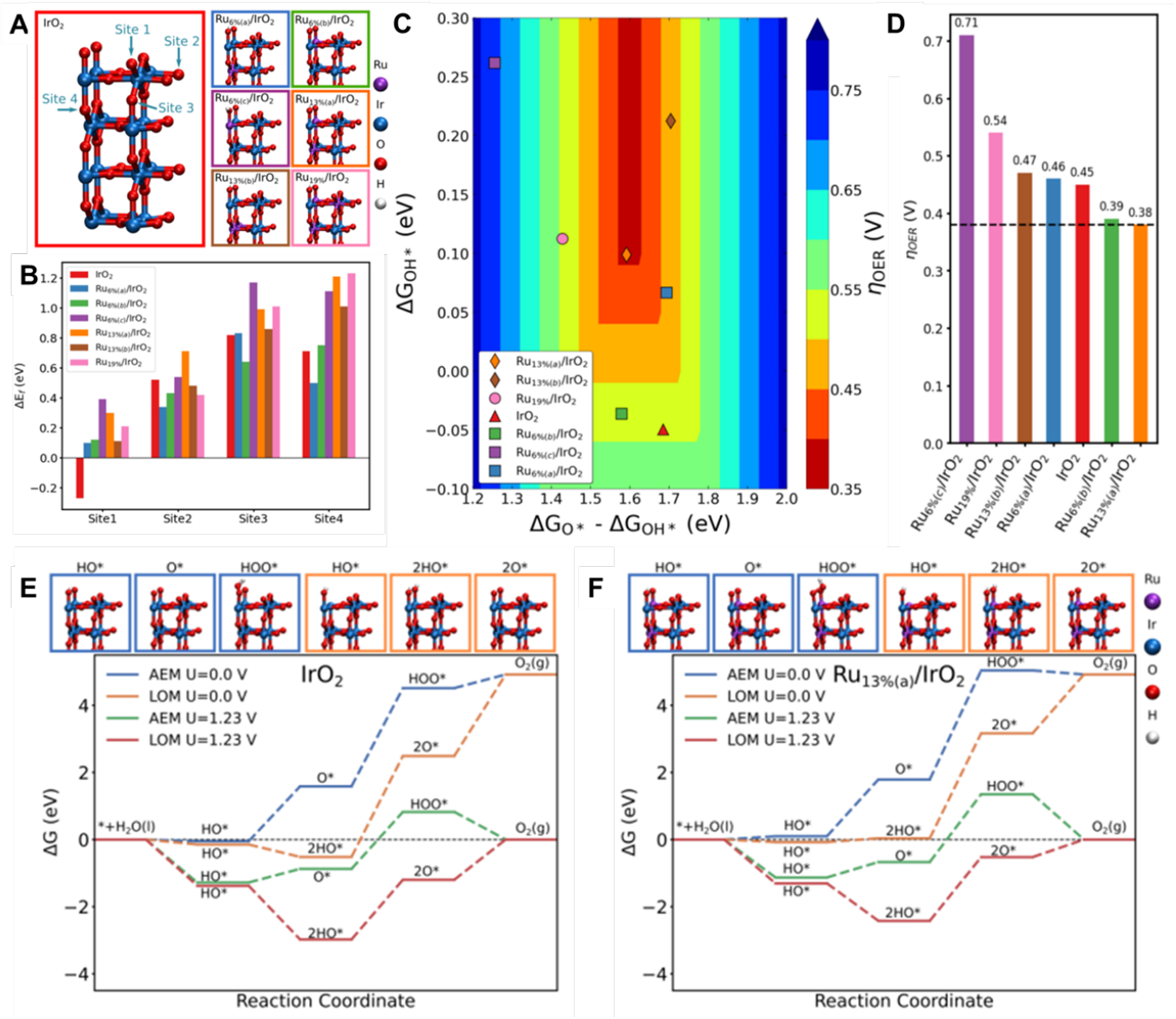

Figure 6. Density functional theory calculations. (A) Different Ru_x/IrO_2 loading systems at various sites. Arrows are used to indicate four specific sites for Ir doping. (B) Calculated formation energy of an oxygen vacancy for different Ru_x/IrO_2 loading systems at various sites; A negative value indicates that vacancy formation is energetically favorable. The model systems include pure IrO_2, $Ru_{6\%(a-c)}/IrO_2$, $Ru_{13\%(a,b)}/IrO_2$, and $Ru_{19\%}/IrO_2$. (C) Volcano plot of the OER overpotential as a function of adsorption free energies, ΔG_{HO*} and ΔG_{O*}, for reaction intermediates. (D) Theoretical overpotential, η_{OER}, for different Ru_x/IrO_2 loading. (E-F) Free energy diagrams of IrO_2 (E) and $Ru_{13\%(a)}/IrO_2$ (F) depicting the adsorbate evolution mechanism (AEM) and lattice-oxygen-mediated mechanism (LOM) for the OER at U=0 V, and U = 1.23 V standard potential, pH=0, and T=298 K. Key intermediate structures for both AEM and LOM pathways are shown on top. Atom colors are indicated.

Taking the AEM pathway on IrO_2 at U = 0.0 V, we find that the initial step involves the exothermic adsorption of HO* on the IrO_2 surface (**Fig. 6E**). The subsequent oxidation of HO* to O* is an uphill process with a

thermodynamic barrier of 1.63 eV, followed by an oxidation of additional H_2O molecule and O* to form HOO* with a barrier of 2.93 eV. The free energy diagram at U = 1.23 V, shows that the most uphill step (also known as thermodynamic barrier) for the OER following the AEM is associated with the oxidation of O* to HOO*. The free energy diagram for the LOM pathway starts with the adsorption of H_2O(l) and a subsequent oxidation leading to the formation of HO*. The next step in LOM pathway diverges from AEM as another H_2O molecule needs to be oxidized and form the second HO* in a second active site, followed by an oxidation of both HO*s to 2O*, resulting in the formation of O_2(*g*). The thermodynamic barrier in LOM is energetically competitive with its counterpart in the AEM pathway. However, the occurrence of two exothermic steps at the onset implies that LOM could potentially offer a more advantageous route in IrO_2 when contrasted with AEM. This observation aligns with recent experimental findings reported for IrO_2 using in-situ operando experiments[32] and explains why IrO_2 has a significant increase in lattice oxygen content after OER (XPS analysis, **Fig. S11**).

For the $Ru_{13\%(a)}/IrO_2$ system (**Fig. 6F**), the LOM and AEM mechanisms closely mirror that of IrO_2, sharing the same key intermediates. The most apparent difference in the LOM pathway is that the introduction of a Ru single atom weakens the adsorption free energy of the second HO* on Ir sites, which in turn results in a lower overpotential. In the AEM, the highest thermodynamic barrier still remains to be the oxidation of O* to HOO*. In the LOM pathway, there is a slightly exothermic adsorption of HO* with an energy gain of 0.076 eV. However, subsequent steps in the LOM pathway are uphill, resembling the energy profile observed in the AEM pathway. Notably, the thermodynamic barrier at U = 1.23 V for oxidation of 2HO* to 2O* is slightly higher than the corresponding barrier in the IrO_2 system.

At U = 1.23 V for the AEM, going from O*+H_2O to HOO* is accompanied by 1.70 eV and 2.02 eV on IrO_2 and $Ru_{13\%(a)}/IrO_2$, respectively. Conversely, the LOM mechanism has thermodynamic barriers of 1.78 eV and 1.9 eV on IrO_2 and $Ru_{13\%(a)}/IrO_2$, for oxidation of 2HO* to 2O*. These results suggest that while there is a competition between AEM and LOM in both IrO_2 and $Ru_{13\%(a)}/IrO_2$, LOM is potentially less favorable when Ru is doped into the IrO_2. This entails the higher stability for Ru_x/IrO_{2-x} catalysts which is consistent with experimental observations from XPS results where the lattice oxygen content (an indicator of abundant oxygen vacancies) is less impacted or reduced for after OER test (**Fig. S11**).

While our mechanistic analysis focuses primarily on the competition between the AEM and the LOM, we acknowledge that other OER pathways have been proposed in the literature for IrO_2, including peroxo-based oxygen coupling, dual-site mechanisms, and proton-coupled electron transfer (PCET) variants. Notably, recent theoretical works by Ha and Larsen[41], Goddard and Ping[42], Binninger and Doublet[43], and Krewer et al[44] have broadened the mechanistic landscape by identifying multiple coexisting or condition-dependent pathways. However, our combined experimental and theoretical strategy is designed to investigate the specific interplay between AEM and LOM, as these are the two mechanisms most strongly implicated by our operando spectroscopic data (**Fig. 3** and **Fig. S15**). XPS and EXAFS analyses indicate that lattice oxygen redox activity and oxygen vacancy evolution correlate directly with catalytic stability in our Ru-doped IrO_2 system (**Fig. 2** and **Fig.**

S11). Since LOM is closely tied to catalyst degradation via lattice oxygen participation and Ir dissolution, our DFT calculations were constructed to quantify how Ru incorporation shifts the mechanistic preference away from LOM and toward AEM. While we do not dismiss the possibility that other pathways may operate under specific electrochemical conditions, our study prioritizes the thermodynamically and experimentally dominant pathways most relevant to explaining the stability and reactivity trends observed in our system. To reflect the broader context, we have now expanded the discussion to acknowledge the mechanistic diversity of OER on IrO_2 and position our AEM–LOM analysis as a stability-driven exploration supported by both theory and experiment.

It is important to note that the computational analysis presented in this work, based on the CHE model, is primarily applicable to reaction energetics in the kinetic regime of oxygen evolution, typically corresponding to low-to-moderate overpotentials. While the CHE model has proven widely effective for identifying intrinsic catalytic trends and theoretical overpotentials, it does not capture electrochemical phenomena that become prominent at high current densities, such as mass transport limitations, interfacial potential gradients, double-layer effects, or solvent reorganization. Our DFT calculations are therefore intended to provide atomistic-level insights into the impact of Ru incorporation on the electronic structure and thermodynamics of IrO_x surfaces, rather than simulate the full electrochemical environment at industrial current densities. At such large driving forces, additional modeling frameworks—such as continuum-level transport simulations, kinetic Monte Carlo (KMC) methods, or Marcus theory-based solvent interaction models—may be necessary to fully describe the electrochemical response. We acknowledge this limitation and have indicated that while our findings are not directly transferable to the mass-transport-limited regime, they nonetheless offer meaningful mechanistic insights into catalyst stability and activity trends under relevant reaction conditions.

Conclusions

In conclusion, we developed a confinement reconstruction strategy for OER catalysts in neutral CO_2 electrolysis using MEA reactor, achieving high activity and stability. EG served as a structural modulator, protecting the catalyst surface and promoting an ordered reconstruction. Ru acted as a dual-function regulator, stabilizing IrO_2 by forming robust Ir–O–Ru bridging structures, which facilitated the transition from 4-fold to 6-fold symmetry, enhancing structural rigidity. Simultaneously, Ru modulated the oxidation state of Ir, optimizing the electronic structure and improving the stability of active sites. The Ru0.05mg/IrO_x catalyst maintained stable operation at 200 mA cm^{-2} for 480 h accompanied by over 80% CO FE in MEA-based CO_2 electrolysis. DFT calculations confirmed that Ru suppressed oxygen vacancy formation and enhanced activity, making the AEM more favorable. This strategy provided new insights into high-current-density OER catalyst design, accelerating the commercialization of CO_2 electrolysis in neutral electrolytes.

Data availability

The authors declare that all data supporting this study are available within the paper and Supplementary Information files. Source data are provided with this paper.

Code availability

All the DFT calculations were performed using the commercial software VASP. All the input and output files of the calculations are available per request.

Acknowledgement

Y.A. W thanks the funding from the Government of Canada's New Frontiers Research Fund-Transformation CANSTOREnergy Project NFRFT-2022-00197, Tang Family Chair in New Energy Materials and Sustainability, the Natural Sciences and Engineering Research Council of Canada (NSERC) (RGPIN-2020-05903, GECR-2020-00476), Canadian Foundation for Innovation John R. Evans Leaders Fund (#41779), and Ontario Research Fund for Small Infrastructure (#41779). This research used resources of the Canadian Light Source and its funding partners. These works for STXM, SM, and Far-IR beamlines of the Canadian Light Source (CLS), a national research facility of the University of Saskatchewan, which is supported by the Canada Foundation for Innovation (CFI), the Natural Sciences and Engineering Research Council (NSERC), the National Research Council (NRC), and the Canadian Institutes of Health Research (CIHR), and the Government of Saskatchewan. Scanning Transmission Electron microscopy was performed at the Canadian Centre for Electron Microscopy (also supported by NSERC and other government agencies). This research was performed on APS beam time award (https://doi.org/10.46936/APS-183348/60011351) from the Advanced Photon Source, a U.S. Department of Energy (DOE) Office of Science user facility operated for the DOE Office of Science by Argonne National Laboratory under Contract No. DE-AC02-06CH11357, and the Canadian Light Source and its funding partners. The authors also acknowledge the computational resources and technical support provided by Advanced Research Computing (ARC) Services group at the University of Calgary and the Digital Research Alliance of Canada (alliancecan.ca). O.L.E. acknowledges the funding from the Canada First Research Excellence Fund (CFREF) program. S.S. acknowledges the support from Natural Sciences and Engineering Research Council (NSERC) of Canada (Discovery Grant No. RGPIN-2023-05298).

Author contributions

Y.A.W. conceived and supervised the experimental research. S.S. conceived and supervised the computational research. L.W., S.L., and C.D. carried out the catalyst's synthesis, characterization, and performance test. O.L.E., A. S., and S.S. performed the DFT calculations. X.W., M.W., H.Z., and C.J.S. carried out the *ex situ* XAS measurements and data fitting. H. W., J. Z., and J. W. performed the STXM measurements. B. K. helped with ICP measurement. S. L., Z. S., and R. D. L. S. performed in situ Raman measurements. W. W., B. Z. and Z. C. assisted with materials characterizations. A.T., and B.B. helped with FT-IR test. D. S. involved in valuable discussions. L.W., O.L.E, S.S. and Y.A.W. wrote the manuscript. All authors made comments and revised the manuscript.

Competing interests

The authors declare the following competing interests: Y.A.W., S.L., C.D., have filed a patent application (US Patent Application number 19/067, 648) on this technology. The remaining authors declare no competing interests.

Supporting information

The Supporting Information is available free of charge.

It includes SEM images, AC-HAADF-STEM images, EELS maps, and XPS spectra for IrO_x, IrO_x-EG and Ru0.05mg/IrO_x before and after reaction; Experimental and fitting spectra of Ir L_3-edge; EXAFS fitting parameters at the Ir K-edge for various samples; Experimental and fitting spectra of Ru K-edge; EXAFS fitting parameters at the Ru K-edge for various samples; Wavelet transforms for k^3-weighted EXAFS signals of Ir L_3-edge and Ru K-edge; The results of ICP-MS analysis of as-prepared samples on Ti felt before and after reaction; In situ real-time ATR FT-IR spectra of the Ru0.05mg/IrO_x sample; In situ Raman test of IrO_x; Comparison of LSV curves of IrO_x and IrO_x-EG after 12h stability test at different current densities; LSV curves normalized by the geometric area for all samples before stability test; The 12-hour stability test for Ru/IrO_x with varying Ru loadings; Comparison of LSV curve; LSV curves normalized by the geometric area for all samples after stability test; Electrochemical active surface area tests (ECSA) and electrochemical double-layer capacity (C_{dl}) for IrO_x and samples with different Ru loadings; LSV curves normalized by ECSA; The eCO_2RR stability test of Ru0.05mg/IrO_x@Ag NPs under acidic media.

References

1. Bushuyev, O. S., et al., What should we make with CO2 and how can we make it? *Joule.* 2018**,** *2* (5), 825-832.
2. Nitopi, S., et al., Progress and perspectives of electrochemical CO2 reduction on copper in aqueous electrolyte. *Chem. Rev.* 2019**,** *119* (12), 7610-7672.
3. Song, Y., et al., Surface Activation by Single Ru Atoms for Enhanced High-Temperature CO2 Electrolysis. *Angew. Chem.,Int. Ed***.** 2024**,** *63* (5), e202313361.
4. Chen, C., et al., Address the “alkalinity problem” in CO2 electrolysis with catalyst design and translation. *Joule.* 2021**,** *5* (4), 737-742.
5. O’Brien, C. P., et al., CO2 Electrolyzers. *Chem. Rev.* 2024.
6. Zhang, Z., et al., Membrane electrode assembly for electrocatalytic CO2 reduction: principle and application. *Angew. Chem.* 2023**,** *135* (28), e202302789.
7. Wang, L., et al., Stabilized Cuδ+-OH species on in situ reconstructed Cu nanoparticles for CO2-to-C2H4 conversion in neutral media. *Nat. Commun.* 2024**,** *15* (1), 7477.
8. Zheng, T., et al., Large-scale and highly selective CO2 electrocatalytic reduction on nickel single-atom catalyst. *Joule.* 2019**,** *3* (1), 265-278.
9. Li, K., et al., In situ dynamic construction of a copper tin sulfide catalyst for high-performance electrochemical CO2 conversion to formate. *ACS Catal.* 2022**,** *12* (16), 9922-9932.
10. Xu, J., et al., IrO x· n H2O with lattice water–assisted oxygen exchange for high-performance proton exchange membrane water electrolyzers. *Sci. Adv.* 2023**,** *9* (25), eadh1718.
11. Gabardo, C. M., et al., Continuous carbon dioxide electroreduction to concentrated multi-carbon products using a membrane electrode assembly. *Joule.* 2019**,** *3* (11), 2777-2791.

12. Chen, J., et al., Cobalt-doped Ru@ RuO2 core–shell heterostructure for efficient acidic water oxidation in low-Ru-loading proton exchange membrane water electrolyzers. *J. Am. Chem. Soc.* 2025**,** *147* (10), 8720-8731.
13. Oh, H.-S., et al., Electrochemical catalyst–support effects and their stabilizing role for IrO x nanoparticle catalysts during the oxygen evolution reaction. *J. Am. Chem. Soc.* 2016**,** *138* (38), 12552-12563.
14. Claudel, F., et al., Degradation mechanisms of oxygen evolution reaction electrocatalysts: a combined identical-location transmission electron microscopy and X-ray photoelectron spectroscopy study. *ACS Catal.* 2019**,** *9* (5), 4688-4698.
15. Yu, H., et al., Microscopic insights on the degradation of a PEM water electrolyzer with ultra-low catalyst loading. *Appl. Catal. B: Environ.* 2020**,** *260*, 118194.
16. Jiang, B., et al., Efficient oxygen evolution on mesoporous IrO x nanosheets. *Catal. Sci. Technol.* 2019**,** *9* (14), 3697-3702.
17. Qi, J., et al., Understanding the stabilization effect of the hydrous IrO x layer formed on the iridium oxide surface during the oxygen evolution reaction in acid. *Inorganic Chemistry Frontiers***.** 2023**,** *10* (3), 776-786.
18. Bhattacharyya, K., et al., Structure and reactivity of IrO X nanoparticles for the oxygen evolution reaction in electrocatalysis: an electronic structure theory study. *J. Phys. Chem. C.* 2021**,** *125* (8), 4379-4390.
19. Tian, C., et al., Evaluating the effect of oxygen vacancies on the OER activity of LaNiO3. 2024.
20. Hirai, S., et al., Oxygen vacancy-originated highly active electrocatalysts for the oxygen evolution reaction. *J. Mater. Chem. A.* 2018**,** *6* (31), 15102-15109.
21. Dong, Y., et al., Atomically dispersed Ru doped on IrO x sub-nanoclusters for enhanced oxygen evolution reaction in acidic media. *J. Mater. Chem. A.* 2024**,** *12* (33), 21905-21911.
22. Shen, S., et al., Advancements and challenges of industrial-level acidic CO2 electrolysis. *MetalMat***.** 2024**,** *1* (2), e28.
23. Peng, L., et al., Research advances in electrocatalysts, electrolytes, reactors and membranes for the electrocatalytic carbon dioxide reduction reaction [J]. *Acta Phys. -Chim. Sin.* 2023**,** *39* (12), 2302037.
24. Qiu, C., et al., Low-iridium stabilized ruthenium oxide anode catalyst for durable proton-exchange membrane water electrolysis. *Nat. Nanotechnol.* 2025, 1-9.
25. Zhang, Y., et al., Electrodeposited nanometer-size IrO2/Ti electrodes with 0.3 mg IrO2 cm−2 for sludge dewatering electrolysers. *Electrochimica acta***.** 2018**,** *265*, 507-513.
26. Li, L., et al., Stable, active CO2 reduction to formate via redox-modulated stabilization of active sites. *Nature communications***.** 2021**,** *12* (1), 5223-5223.
27. Kresse, G.; Furthmüller, J., Efficiency of ab-initio total energy calculations for metals and semiconductors using a plane-wave basis set. *Computational materials science***.** 1996**,** *6* (1), 15-50.
28. Kresse, G.; Furthmüller, J., Efficient iterative schemes for ab initio total-energy calculations using a plane-wave basis set. *Physical review. B, Condensed matter***.** 1996**,** *54* (16), 11169-11186.
29. Hjorth Larsen, A., et al., The atomic simulation environment-a Python library for working with atoms. *Journal of physics. Condensed matter***.** 2017**,** *29* (27), 273002-273002.
30. Perdew, J. P., et al., Generalized Gradient Approximation Made Simple. *Physical review letters***.** 1996**,** *77* (18), 3865-3868.
31. Blöchl, P. E., Projector augmented-wave method. *Physical review. B, Condensed matter***.** 1994**,** *50* (24), 17953-17979.
32. G Kresse, D. J., From ultrasoft pseudopotentials to the projector augmented-wave method. *Physical review b***.** 1999**,** *59* (1758).
33. Jain, A., et al., Commentary: The Materials Project: A materials genome approach to accelerating materials innovation. *APL materials***.** 2013**,** *1* (1), 011002-011002-011011.
34. Siahrostami, S.; Vojvodic, A., Influence of adsorbed water on the oxygen evolution reaction on oxides. *J. Phys. Chem. C.* 2015**,** *119* (2), 1032-1037.
35. Shan, J., et al., Charge-redistribution-enhanced nanocrystalline Ru@ IrOx electrocatalysts for oxygen evolution in acidic media. *Chem***.** 2019**,** *5* (2), 445-459.

36. Oh, A., et al., Topotactic transformations in an icosahedral nanocrystal to form efficient water-splitting catalysts. *Adv. Mater.* 2019**,** *31* (1), 1805546.
37. Guo, R., et al., Activating the passivated Ir sites in 3R-IrO2 by intercalating Pt atoms for enhanced oxygen reduction reaction activity. *Chem. Eng. J.* 2024**,** *484*, 149671.
38. Quan, L., et al., Bifunctional electrocatalysts for overall and hybrid water splitting. *Chem. Rev.* 2024**,** *124* (7), 3694-3812.
39. Lin, C., et al., In-situ reconstructed Ru atom array on α-MnO2 with enhanced performance for acidic water oxidation. *Nat. Catal.* 2021**,** *4* (12), 1012-1023.
40. Li, L., et al., Lanthanide-regulating Ru-O covalency optimizes acidic oxygen evolution electrocatalysis. *Nat. Commun.* 2024**,** *15* (1), 4974.
41. Ha, M.-A.; Larsen, R. E., Multiple reaction pathways for the oxygen evolution reaction may contribute to IrO2 (110)'s high activity. *J. Electrochem. Soc.* 2021**,** *168* (2), 024506.
42. Ping, Y., et al., The reaction mechanism with free energy barriers at constant potentials for the oxygen evolution reaction at the IrO2 (110) surface. *J. Am. Chem. Soc.* 2017**,** *139* (1), 149-155.
43. Binninger, T.; Doublet, M.-L., The Ir–OOOO–Ir transition state and the mechanism of the oxygen evolution reaction on IrO 2 (110). *Energy Environ. Sci.* 2022**,** *15* (6), 2519-2528.
44. Geppert, J., et al., Microkinetic analysis of the oxygen evolution performance at different stages of iridium oxide degradation. *J. Am. Chem. Soc.* 2022**,** *144* (29), 13205-13217.

TOC graphic